

Alma Mater Studiorum Università di Bologna
Archivio istituzionale della ricerca

Performance analysis and optimal sizing of electric multirotors

This is the final peer-reviewed author's accepted manuscript (postprint) of the following publication:

Published Version:

de Angelis E.L., Giulietti F., Rossetti G., Bellani G. (2021). Performance analysis and optimal sizing of electric multirotors. AEROSPACE SCIENCE AND TECHNOLOGY, 118, 1-15 [10.1016/j.ast.2021.107057].

Availability:

This version is available at: <https://hdl.handle.net/11585/844724> since: 2024-08-30

Published:

DOI: <http://doi.org/10.1016/j.ast.2021.107057>

Terms of use:

Some rights reserved. The terms and conditions for the reuse of this version of the manuscript are specified in the publishing policy. For all terms of use and more information see the publisher's website.

This item was downloaded from IRIS Università di Bologna (<https://cris.unibo.it/>).
When citing, please refer to the published version.

(Article begins on next page)

Performance Analysis and Optimal Sizing of Electric Multirotors

Emanuele L. de Angelis^{*,1}, Fabrizio Giulietti², Gianluca Rossetti³, Gabriele Bellani⁴

University of Bologna, Forlì, Italy 47121

Abstract

This paper presents an analytical framework for addressing the hovering performance of a battery-powered multirotor. The estimation of power required for flight is investigated and an analytical model is proposed to describe the rotor figure of merit as a function of few relevant blade parameters, without the need for ad hoc experiments. The model is derived after a discussion about the aerodynamics of rotating blades. The formulation in terms of Reynolds number is supported by an experimental campaign, performed on a set of commercial-of-the-shelf propellers optimized for small-scale multirotor applications.

By imposing the balance between required and available power, the hovering time is predicted by an integral formulation developed for a constant-power battery discharge process. The best endurance condition is obtained in terms of optimum battery capacity and flight time. The methodology, applicable to the design phase of novel multirotor configurations, is finally validated by flight tests.

^{*}Corresponding author

¹Research Fellow, Department of Industrial Engineering (DIN), emanuele.deangelis4@unibo.it

²Associate Professor, Department of Industrial Engineering (DIN), fabrizio.giulietti@unibo.it

³Research Fellow, Interdepartmental Center for Industrial Research (CIRI Aerospace), gianluca.rossetti3@unibo.it

⁴Assistant Professor, Department of Industrial Engineering (DIN), gabriele.bellani2@unibo.it

1. Introduction

Remotely-Piloted Aerial Systems (RPAS), particularly small battery-powered fixed and rotary-wing platforms, gained a large interest in the scientific community. Reduced size, weight, and operational costs, in fact, make such systems one of the most suitable solutions for a wide range of applications, including load transportation, search and rescue, risk management, surveillance, aero-photogrammetry, and, in general, remote sensing activities [1, 2].

Among the available rotary-wing configurations, multirotors proved to be particularly attractive [3]. On the one hand, low structural complexity and simplicity of use allow for operative cost reduction. On the other hand, the hovering and vertical take-off and landing capabilities empower effective operations in restricted and obstructed areas [4, 5]. Also, with respect to a conventional helicopter with the same take-off weight, a multirotor is typically characterized by a more compact size, with satisfactory robustness to external disturbances and improved maneuvering capabilities [6, 7]. Such features are achieved by spreading the total disc area into multiple propulsion units, where the use of smaller propellers rotating at a higher speed comes at the cost of a loss in efficiency with respect to the conventional, single-rotor configuration. This, in addition to the limited endurance-to-weight ratio typical of electrically-driven systems, makes the performance of the hovering condition a critical, but challenging, issue. In this respect, the larger demand for high endurance RPAS operations, has increased the interest on research programs which aim at deriving numerical and analytical tools for range/endurance prediction and optimal preliminary sizing [8].

1 Most of the available multirotor configurations use MH-Ni, Li-Po, and
2 Li-Ion battery packs. Due to their long life, small self-discharge, and high
3 energy-to-weight ratio, Li-Po and Li-Ion systems have become the most
4 widespread solution to power supply, provided a suitable Battery Manage-
5 ment System (BMS) is designed to ensure safety and efficiency of battery
6 usage [9]. The basic functions of a BMS include battery data acquisition,
7 modeling and state estimation, charge and discharge control, fault diagnosis
8 and alarm, thermal management, balance control, and communication. Bat-
9 tery modeling and state estimation are thus key functions of advanced BMS,
10 allowing for reliable operation of unmanned systems, optimize the battery
11 configuration, and provide a basis for safety management [10]. The battery
12 models presented in literature mainly fall into the following three categories:
13 a) physics-based electrochemical models [11], b) electrical equivalent circuit
14 models [12], and c) data-driven models established by artificial intelligence
15 algorithms such as neural networks or support vector machines [13]. With re-
16 spect to the battery state estimation problem, different techniques have been
17 proposed in order to characterize the state-of-charge/state-of-energy. These
18 methods include a) the use of look-up tables, b) -hour integral routines, c)
19 recursive algorithms based on Kalman-like [14] or particle filter approaches,
20 d) state-observers, e) data-driven based methods, such as neural networks,
21 fuzzy-logic and genetic algorithms, support vector machines [15].

22 Early studies investigating the performance and sizing of battery-powered
23 aircraft became available only at the beginning of the last decade, based on
24 Peukert's modeling of the discharge process [16]. In particular, numerical and
25 analytical solutions addressing electric aircraft performance are presented

1 in [17], where the effects of absorbed current on residual battery capacity
 2 are considered. In Ref. [18] the best range condition is discussed in detail
 3 while in [19] endurance estimates are validated by means of an experimental
 4 campaign. With regard to multicopter vehicles, a closed-form solution for en-
 5 durance analysis as well as an optimal sizing approach for the battery pack is
 6 provided in [20], where the configuration for maximum endurance is outlined
 7 in terms of rotorcraft design features and optimal battery capacity, after a
 8 test-bed characterization of the powerplant. Lindahl et al. [21] propose a
 9 sizing tool to select a good combination of propulsion components, based on a
 10 linear approximation to the ohmic region of the battery discharge law. Using
 11 momentum theory and blade element theory, Latorre [22] offers an optimal
 12 design for the electric power system of a quadrotor using the identification
 13 method, and proposes a mathematical model to select the optimal motor.
 14 Kaya et al. [23] use a polynomial model to estimate the motor-propeller pair
 15 performance (from the endurance point of view), based on collected test data
 16 and under the assumption of constant current discharge. By introducing the
 17 notions of available capacity and usable capacity factors, Abdilla et al. [24]
 18 obtain an endurance formula model for rotorcraft driven by Li-Po batter-
 19 ies. The same authors finally propose a technique to optimize the endurance
 20 of rotorcraft by sub-dividing the monolithic battery into multiple smaller-
 21 capacity batteries, which are then sequentially discharged and released [25].

22 The above mentioned approaches, typically based on Peukert's equation,
 23 stem from the simplifying assumption of a constant-current discharge model.
 24 However, it must be noted that a constant-power battery discharge process is
 25 more representative of fixed-wing steady-level flight or hovering of battery-

1 powered rotorcraft. To this aim, Fuller [26] developed a battery discharge
2 model, based on a modification of Peukert’s law, to predict the terminal
3 voltage and current for a constant–power process. Finally, a novel constant–
4 power integral formulation of battery discharge process was derived, based
5 on experimental data, in Ref. [27] by some of the present authors. This
6 model provides a complete framework for performance analysis and optimal
7 preliminary sizing of fixed–wing platforms.

8 In order to fully predict and optimize the performance of electric rotor-
9 craft, however, battery modeling is only the starting point. The complete
10 propulsion system needs to be characterized, with particular attention to the
11 generation of thrust from selected propellers. In Ref. [28] the aerodynamic
12 efficiency of small–scale propellers is addressed also under non–axial inflow
13 conditions, whereas in [29] a mathematical model of the engine thrust/RPM
14 function for low Reynolds number applications is presented. With respect
15 to multicopter sizing, recent works address the problem by means of scaling
16 laws and similarity models [30], and by using a hybrid approach which in-
17 tegrates theoretical formulations, computational fluid dynamics, and exper-
18 imental validation [31, 32, 33]. Other approaches to the throttle/thrust and
19 thrust/power functions description are obtained by experimental validations
20 [34, 35], manufacturer data [36], or CFD analysis [37].

21 In what follows, the total power required for the hovering condition is
22 calculated according to the procedure presented in [38]. Then, in order to
23 characterize the aerodynamic behavior of the propeller, an analytical model
24 is proposed to describe the rotor figure of merit as a function of few relevant
25 blade parameters. To this aim, results of the classical Blade Element (Mo-

1 momentum) Theory (BET) [39] are enhanced by introducing an empirical cor-
2 rection function allowing for a more accurate prediction of the required blade
3 tip speed, for a given thrust condition. Following a similar approach, a semi-
4 empirical expression of the figure of merit as a function of blade Reynolds
5 number [40] and propeller pitch/diameter ratio is finally derived. These re-
6 sults are obtained thanks to a dedicated experimental campaign performed on
7 a selection of commercial-of-the-shelf propellers, optimized for small-scale
8 multirotor applications. At the cost of few simplifying assumptions, flight
9 endurance is analytically evaluated according to the battery model presented
10 in [27], adapted for the first time to the analysis of multirotor platforms.

11 Finally, such model is applied to prove the existence of an optimal battery
12 configuration (namely the configuration determining the maximum hovering
13 endurance). In fact, unlike conventional fuel-powered vehicles, where an
14 increased fuel fraction always provides increased endurance and range, the
15 weight of electrically-powered vehicles remains constant. Hence, the bene-
16 ficial effect of weight loss during flight is not experienced [20]. In this case,
17 increasing battery weight may not necessarily provide an increased endurance
18 and/or range, if the energy cost of lifting more weight overcomes the bene-
19 fit of the increased battery-pack capacity. Generally speaking, the solution
20 to the optimal sizing of battery packs is a challenging issue, which involves
21 different kinds of electric vehicles. Wang et al. [41] prove that the range-
22 and energy-optimal design points can be considered concurrently in design
23 optimization of small electric aircraft: for a given flight task and performance
24 objective, the approach incorporating the dynamic battery model and static
25 component model provides an optimal flight trajectory and the correspond-

1 ing battery package parameters. In [42] convex modeling steps are introduced
2 to simultaneously optimize battery sizing and energy management of hybrid
3 electric vehicle powertrains. An investigation is also provided where results
4 from convex optimization are compared to those obtained with dynamic pro-
5 gramming. In [43] the joint optimization problem of battery mass and flight
6 trajectory for high-altitude solar-powered aircraft is discussed. In particu-
7 lar, a Gauss pseudo-spectral method is employed to determine the minimal
8 power consumption while following the flight trajectory, and particle swarm
9 optimization is used to calculate the optimal battery mass. In the present
10 work, the optimal sizing problem is also discussed. Provided that the field
11 of applicability is restricted to the hovering flight condition of a prescribed
12 empty-operative platform, the discharge model presented in [27] is manip-
13 ulated to provide the optimal battery capacity as an analytical function of
14 rotorcraft parameters and battery coefficients. Predictions from this model
15 are validated with a few test cases.

16 The major contribution of the present paper to multirotor aircraft state-
17 of-the-art is the derivation of a fully analytical framework, based on a re-
18 duced set of relevant design features, without the need of ad hoc laboratory
19 tests on power plant components and battery packs. Almost all the above
20 mentioned approaches to rotors' performance analysis are, in fact, based on
21 the experimental characterization of the entire propulsion chain (battery,
22 regulator, engine, propeller), with particular focus on aerodynamic analysis.
23 Thus, in order to obtain an accurate estimation of rotorcraft performance
24 as well as a suitable preliminary sizing, the actual power system needs to
25 be selected and available for laboratory test campaign. This makes such

1 approaches not applicable when the platform design process is at an early
 2 conceptual stage and the power system selection is the main expected out-
 3 put. To the best of the authors' knowledge, an analytical procedure aimed
 4 at accurately estimating the endurance and range of a multirotor platform
 5 as a function of a reduced number of design parameters is still missing in
 6 the literature. The scope of the present paper is thus to fill this gap by
 7 proposing an analytical approach allowing for an accurate and physically
 8 consistent estimation of multirotor hovering endurance, based on a limited
 9 number of design features, propeller characteristics, and battery parameters.
 10 In this respect, the derived closed-form expression for the figure of merit
 11 allows for the following three main results: 1) rotorcraft accurate power and
 12 endurance prediction at hover, 2) optimal endurance condition analysis, and
 13 3) rotorcraft sizing by providing the optimal battery pack/take-off weight
 14 ratio.

15 The paper is structured as follows. Sections 2 and 3 address the total
 16 power required for the hovering flight and the figure of merit characterization,
 17 respectively. The analytical framework for multirotor endurance prediction
 18 and optimal sizing procedure is derived in Section 4. Numerical simulations
 19 and experimental results validating the proposed technique are finally pre-
 20 sented Section 5. A section of concluding remarks ends this paper.

21 **2. Power Required at Hover**

22 Consider a multirotor with N identical electric motors and propellers,
 23 the latter characterized by a number B of blades. A planar non-ducted non-
 24 intermeshing configuration is analyzed where the thrust generated by each
 25 rotor is aligned with the local vertical when the vehicle is at hover. Extension

1 to a non-planar configuration is straightforward and can be obtained from
 2 the analysis in [6].

3 The total power required for flight,

$$P_r = P_s + P_h \quad (1)$$

4 is expressed as the sum of two main contributions [38], namely the power
 5 to be absorbed by onboard systems, P_s , and the power necessary for the
 6 hovering condition, P_h . The former, allocated to avionics and payload, is
 7 assumed to be approximately constant. The latter, related to the generation
 8 of thrust, is calculated as $P_h = N P_{sh}$, where $P_{sh} = P_{id}/f$ is the power
 9 delivered by each electric motor to its rotor shaft, obtained by dividing the
 10 ideal induced power P_{id} by the rotor figure of merit $f < 1$. Provided m
 11 is the rotorcraft mass and g is the gravitational acceleration, let $W = m g$
 12 be the take-off weight. On the basis of momentum theory, $P_{id} = T v_i$ is
 13 obtained as the product between the thrust generated by the single rotor at
 14 hover, $T = W/N$, and the induced speed v_i , assumed to be uniform on the
 15 actuator disk. According to Glauert's hypothesis [44], the induced velocity
 16 is expressed as a function of rotor thrust, $v_i = \sqrt{T/(2\rho A)}$, where ρ is air
 17 density, $A = \pi R^2$ is rotor disc area, and R is rotor radius. The effect of the
 18 rotor induced velocity on the airframe drag, which would be included in the
 19 computation of P_h , is disregarded in the present framework.

20 The power output of the battery delivered to the propulsion system is
 21 reduced by losses within the electric driving system made of cables, electronic
 22 speed controllers (ESCs), and electric motors. Although each element has its
 23 own efficiency, η_c , η_{esc} , and η_m , respectively, for the purpose of the present
 24 work they are combined into an overall electrical efficiency, $\eta_e = \eta_c \eta_{esc} \eta_m$,

1 such that

$$\eta_e(P_b - P_s) = P_h \quad (2)$$

2 where P_b is the total power produced by the battery pack(s). Taking into
3 account Eq. (1) and the definition of P_h , the total power requested from the
4 battery for the hovering flight becomes

$$P_b = P_s + N P_{id} / (f \eta_e) \quad (3)$$

5 Note that in a correctly sized propulsion system it is $\eta_e \approx \eta_{esc} \eta_m$, provided
6 that power losses in cables are typically negligible within the overall efficiency
7 analysis. On the converse, the system made of ESCs and motors represents
8 a significant source of inefficiency, with performance that is a function of
9 angular rate, torque, and applied voltage [45, 46]. In order to perform the
10 correct characterization of η_e , specifications are typically provided by sys-
11 tem manufacturers, retrieved from online databases [47, 48], or determined
12 experimentally (see Section 5 for some applicative examples).

13 **3. Figure of merit characterization**

14 The figure of merit characterization is based on a detailed knowledge
15 of the aerodynamic coefficients, whose identification requires complex mea-
16 surements or calculations. In the present framework, the figure of merit is
17 expressed as function of few propeller parameters that can be extracted ei-
18 ther from the propeller datasheet or from simple measurements. Once this
19 expression is identified from basic theoretical considerations, the required
20 correction coefficients are identified that best predict the performance of a
21 class of standard propellers optimized for multicopter applications.

1 3.1. Blade-element theory analysis

2 Let Ω be the rotor angular rate, such that $V_{tip} = \Omega R$ is blade tip speed,
 3 and define the thrust coefficient, $C_T = T/(\rho A V_{tip}^2)$. The figure of merit, as
 4 derived by BET and expressed as a function of C_T , is [39]:

$$f = \frac{\frac{C_T^{3/2}}{\sqrt{2}}}{\kappa_{ind} \frac{C_T^{3/2}}{\sqrt{2}} + \frac{\sigma C_d}{8}} \quad (4)$$

5 where $\sigma = B \bar{c}/(\pi R)$ is rotor solidity (with B being the number of blades
 6 and \bar{c} the blade mean aerodynamic chord), C_d is the airfoil drag coefficient
 7 averaged along the blade, and κ_{ind} is the induced-power correction factor.
 8 This coefficient is derived from rotor measurements or flight tests and it
 9 encompasses a number of non ideal effects, including nonuniform inflow, tip
 10 losses, wake swirl and contraction, blades interference, etc. Although κ_{ind}
 11 depends on several blade parameters and is a function of C_T for a generic
 12 lifting rotor [39], it must be noted that in typical small-scale multirotor
 13 applications C_T has limited variability over the available throttle range (see
 14 Fig. 3.a), especially at high rotational speed, where the design operating
 15 point is typically located [49]. It follows that the resulting small fluctuations
 16 of κ_{ind} have a limited impact on the figure of merit. Therefore, in the present
 17 model κ_{ind} is fairly assumed as a constant.

18 On the other hand, the term related to the profile losses has a larger
 19 impact at small C_T values. Therefore, the attention is focused on the analysis
 20 of the drag coefficient C_d and its detailed expression. To this end, define
 21 $Re = \rho c_{75} V_{75}/\mu$ as the Reynolds number conventionally evaluated at 75%
 22 blade radius [40], where μ is the dynamic viscosity of the air, while c_{75} and

1 $V_{75} = \sqrt{v_i^2 + (0.75 \cdot V_{tip})^2}$ respectively represent the local airfoil chord and
2 the relative airspeed.

3 It is important to stress that in large-scale rotors a reasonable first as-
4 sumption is to consider $C_d = C_{d_0}$, namely a constant independent from
5 Reynolds number, being the flow fully turbulent. Instead, in small-scale
6 rotors, the Reynolds number typically ranges between 10^4 – 10^5 , so that the
7 flow can be assumed to be fully laminar [40] and $C_d = C_d(\text{Re})$. To find an
8 expression for C_d the friction coefficient C_f can be expressed according to
9 Blasius theory as [50]:

$$C_f = 1.328/\sqrt{\text{Re}}. \quad (5)$$

10 Although Eq. (5) is derived for a flat-plate boundary layer at zero pressure
11 gradient, in this regime the expression

$$C_d = 2 C_f, \quad (6)$$

12 obtained considering both sides of the blade-section, results to be a reason-
13 able estimate of the drag coefficient for an airfoil at low angle of attack [51].
14 Therefore Eq. (6) is implemented in the present model to describe Reynolds
15 number effects on the profile losses. On the other hand, effects such as
16 boundary layer growth and separation are neglected under the assumption
17 that each section of the considered blade is purposely designed to work at a
18 limited angle of attack during a hovering condition.

19 In order to characterize the local blade air flow, the blade tip speed (and,
20 hence, C_T) needs be estimated for a given thrust condition. According to
21 linearized aerodynamic theory, the local 2-D blade lift coefficient is written
22 as $C_l = C_{l_\alpha} (\alpha - \alpha_0) = C_{l_\alpha} (\theta - \alpha_0 - \phi)$, where C_{l_α} is the slope of the 2-D lift

1 coefficient, α_0 is the corresponding zero-lift angle, θ is the pitch angle, and ϕ
 2 is the relative inflow angle at a generic airfoil section due to the induced flow.
 3 Although $C_{l\alpha}$ and α_0 may vary according to the local airfoil characteristics
 4 and flow conditions, an average value for both parameters, constant along
 5 the blade, is considered. Furthermore, define y as the radial distance from
 6 the rotational axis and $r = y/R$ as the non-dimensional location along the
 7 blade, such that $r = 0$ at the rotor hub and $r = 1$ at the tip. In this
 8 framework, rotor blades are modeled with a linear twist, such that the pitch
 9 angle takes the form $\theta(r) = \theta_0 + r \theta_{tw}$, where θ_0 is the pitch angle value ideally
 10 extrapolated to $r = 0$ and θ_{tw} is the total blade twist angle (tip minus root
 11 pitch angle). In Ref. [39] it is shown that, if the reference blade pitch angle
 12 (here defined as θ_{75}) is taken at $r = 0.75$, then $\theta(r) = \theta_{75} + (r - 0.75)\theta_{tw}$ and

$$C_T = \frac{1}{2} \sigma C_{l\alpha} \left(\frac{\theta_{75} - \alpha_0}{3} - \frac{\lambda}{2} \right) \quad (7)$$

13 where $\lambda = v_i/V_{tip}$ is rotor inflow ratio. Taking into account Eq. (7) and
 14 rewriting the thrust coefficient as $C_T = 2 (v_i/V_{tip})^2$, it follows:

$$2 \left(\frac{v_i}{V_{tip}} \right)^2 = \frac{1}{2} \sigma C_{l\alpha} \left(\frac{\theta_{75} - \alpha_0}{3} - \frac{v_i}{2 V_{tip}} \right) \quad (8)$$

15 that can be arranged to give

$$2 \sigma C_{l\alpha} (\theta_{75} - \alpha_0) V_{tip}^2 - 3 \sigma C_{l\alpha} v_i V_{tip} - 24 v_i^2 = 0 \quad (9)$$

16 Assuming V_{tip} as the unknown variable, two real distinct solutions are pro-
 17 vided by Eq. (9). After excluding the negative one, the required tip speed,
 18 obtained by BET, results to be a function of the induced velocity v_i as

$$V_{tip}^{BET} = k_{tip} v_i \quad (10)$$

1 where

$$k_{tip} = \frac{1}{4} \left(\frac{1 + \sqrt{1 + \frac{64}{\sigma C_{l\alpha}} \theta_{75}/3}}{\theta_{75}/3} \right) \quad (11)$$

2 is obtained by embedding, for simplicity, α_0 into θ_{75} for profile sections with
3 low mean-camber line curvature. Finally, θ_{75} is estimated as

$$\theta_{75} = \arctan \left(\frac{\Gamma}{0.75 \cdot \pi D} \right) \quad (12)$$

4 where Γ is nominal blade advance pitch, provided by the manufacturer, that
5 indicates the distance traveled by the propeller in one turn in the absence of
6 slip [52].

7 By putting together Eqs. (10), (11), and (12), the thrust coefficient in
8 Eq. (7) becomes:

$$C_T = \sigma \pi \left(\frac{4\Gamma}{9\pi D} - \frac{1}{2k_{tip}} \right) \quad (13)$$

9 where it is assumed $C_{l\alpha} = 2\pi \text{ rad}^{-1}$ and $\theta_{75} \approx \Gamma/(0.75 \cdot \pi D)$.

10 The combination of Eqs. (4), (5), and (13) highlights that, under the
11 assumptions made, the figure of merit nominally depends on two main non-
12 dimensional parameters, namely Γ/D and Re . A third parameter is repre-
13 sented by the solidity ratio σ . However, in typical multirotor applications,
14 σ is found to have a limited variability, with average values in the order of
15 0.1 for two-bladed configurations [36]. Therefore, in this framework f is
16 considered as a function of two non-dimensional parameters only. The goal
17 is to find an analytical function $H = H(f, \Gamma/D, \text{Re}) = f(\Gamma/D)^\alpha \text{Re}^\beta$ that
18 smoothly fits the experimental data. The appropriate choice of α and β will
19 be made on the basis of an iterative procedure that minimizes the order of
20 the polynomial needed to fit the data (as it will be shown in Section 3.2.2).

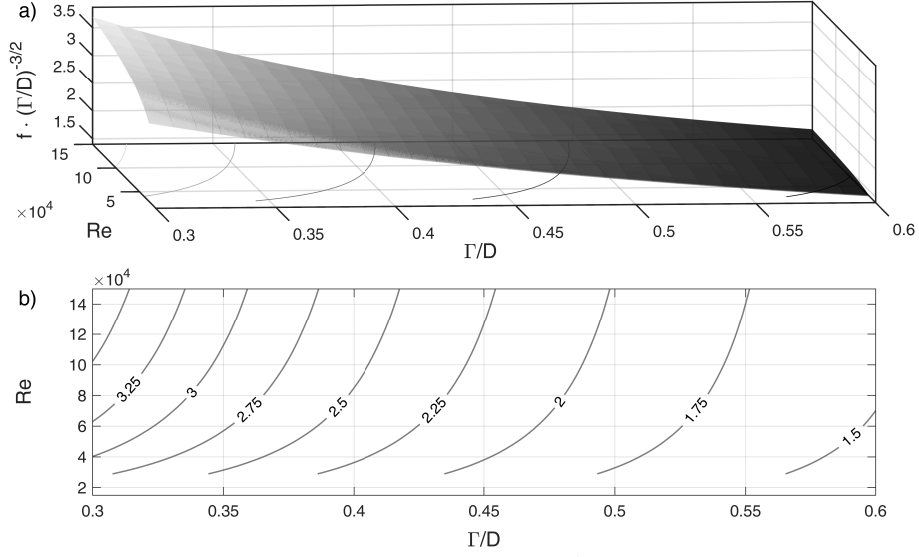


Figure 1: The non-dimensional function $f(\Gamma/D)^\alpha Re^\beta$ as obtained by Eqs. (4), (5), and (13) ($\alpha = -3/2$, $\beta = 0$).

As an example, Fig. 1 shows that for $\alpha = -3/2$ and $\beta = 0$, H is a smooth function of Γ/D and Re . Following Eqs. (4), (5), and (13), the Reynolds number is calculated in standard conditions for a rotation rate Ω in the range $100 - 800$ rad/s. A reference configuration is considered with diameter $D = 15$ in, the value of σ is selected as 0.1, and a constant value of $\kappa_{ind} = 1.25$ is assumed without loss of generality. As the plot shows, the figure of merit increases monotonically with Re . This is a consequence of the monotonic decrease of the drag coefficient with Reynolds number in the range considered here. However, it has to be pointed out that the model in Eq. (10) implies a constant inflow-ratio, with the result that C_T in Eq. (13) does not vary with thrust, for a given value of Γ/D . Conversely, C_T may vary as the Reynolds number increases, due to the increase in angular velocity. This produces a decay of the figure of merit above a certain critical value of

Re, as a consequence of non-ideal flow conditions. This and other effects will be accounted for in the next section, where the ideal model introduced above is re-discussed with the contribution of experimental correction factors.

3.2. Enhanced blade characterization

The general expression for f obtained by Eqs. (4), (5), and (13) is useful to determine the relevant parameters needed to fully describe the figure of merit of a typical multirotor blade. However, this expression is obtained with strong assumptions on the blade and inflow characteristics, such as profile curvature, blade twist configuration, induced velocity distribution, and, in general, all the hypotheses at the base of BET (including the blade spanwise-averaging of aerodynamic properties).

To compensate for these effects, correction factors need to be experimentally determined and introduced in the modeling approach. In this regard, an experimental campaign is conducted with details provided in what follows. All tests are performed on a set of commercial-of-the-shelf propellers, selected on the basis of the following assumption:

Assumption 1 *Static thrust is generated by a two-bladed propeller ($B = 2$) specifically designed for multirotor applications. It is assumed that $0.3 \leq \Gamma/D \leq 0.6$ and $D \leq 16$ in.*

3.2.1. Experimental setup

A total of 9 different propellers, depicted in Figure 2, is selected with characteristics detailed in Table 1.

For each propeller, a static thrust test is performed by a propulsion system made of a T-Motor T40A ESC and a T-Motor Antigravity 4006 KV380 brushless motor. The unit is mounted on a RCbenchmark Series 1585 thrust

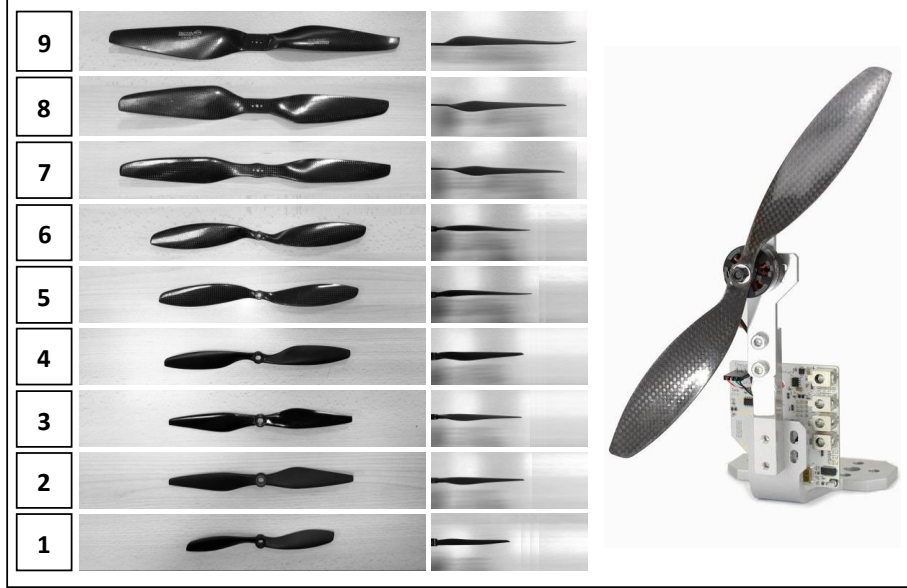


Figure 2: The sample propellers (planform and side views) and a detail of the thrust stand.

stand tailored to small and medium size drone optimization analysis. The test bench supports thrust and torque measurement up to 5 kgf and 1.5 Nm, respectively, and an optical RPM probe for propeller angular rate estimation. The load cells are temperature-compensated and a preliminary calibration procedure allows for accurate measurements over the full operating range. Electrical power required for the propulsion system is delivered by a laboratory power supply stabilized at 24 V DC.

Each experiment is conducted at room temperature $\tau = 24\text{ }^{\circ}\text{C}$ and static pressure $p = 100\,877\text{ Pa}$, with estimated air density $\rho = 1.1827\text{ kg/m}^3$ and air dynamic viscosity $\mu = 18.32 \cdot 10^{-6}\text{ Pa}\cdot\text{s}$. Provided that the control signal is obtained by pulse-width modulation (PWM), the throttle command is progressively incremented from 1000 to 1800, respectively generating zero and maximum thrust, with steady-state measurements taken at intervals of 100.

Table 1: Relevant data of tested propellers (CF: carbon fiber, CFRN: carbon fiber reinforced nylon).

	Propeller	Finish	Material	D [in]	Γ [in]	\bar{c} [mm]	c_{75} [mm]
1	DJI 0845	polish	CFRN	8	4.5	17.6	21
2	DJI 1038	polish	CFRN	10	3.8	21.5	18
3	DJI 1038S	glossy	CFRN	10	3.8	21.5	18
4	DJI 1045	polish	CFRN	10	4.5	22.0	24
5	HobbyKing 1147	glossy	CF	11	4.7	25.3	29
6	HobbyKing 1238	glossy	CF	12	3.8	28.4	31
7	RC Timer 1555	glossy	CF	15	5.5	29.3	30
8	RC Timer 1555C	glossy	CF	15	5.5	34.2	30
9	RC Timer 1655	glossy	CF	16	5.5	33.7	31

For each propeller, the test is repeated 3 times in the same conditions and collected data are used to derive a single averaged curve for each measured quantity. In Figure 3 the results obtained for propellers 5 and 7 are reported as an example, showing the measured thrust coefficient C_T , torque Q , and angular rate Ω as a function of PWM command.

3.2.2. Experimental results and fitting parameters

One important aspect of the model derived in Eq. (10) is that of constant inflow ratio. This implies a constant value of C_T for a given value of Γ/D . As mentioned above, this is not verified in practice. Hence, it is first needed to introduce in the proposed model a correction factor that allows for a variation of the inflow-ratio with V_{tip} .

Let ξ be a correction factor to the theoretically estimated tip speed V_{tip}^{BET} in Eq. (10), such that $V_{tip} = \xi V_{tip}^{BET}$, where V_{tip} is obtained by direct measurement. In Figure 4 the non-dimensional quantity $g \triangleq \xi \cdot (\Gamma/D)^2 / \sigma$ is plotted as a function of Γ/D and the induced speed v_i for all $V_{tip}^{BET} \neq 0$. The

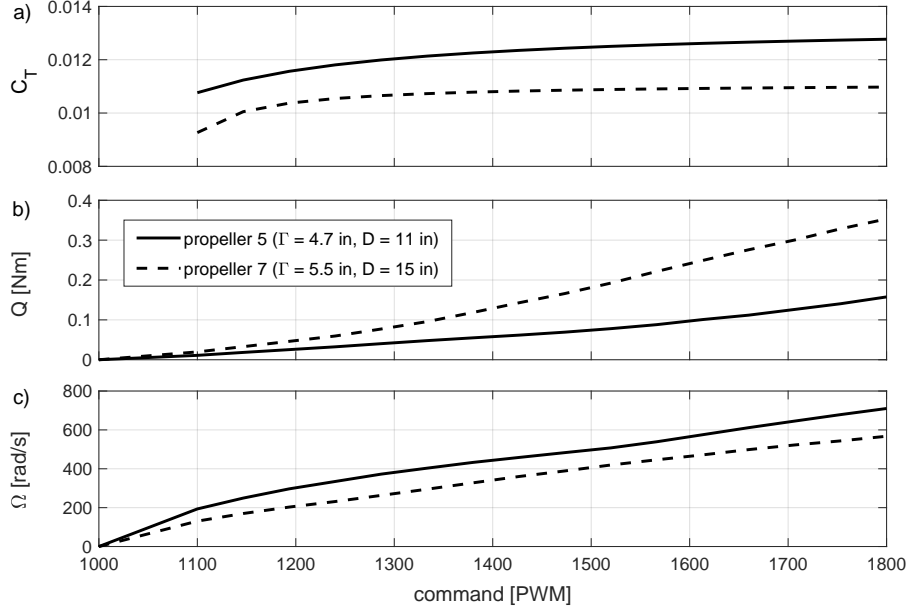


Figure 3: Measurements obtained for propellers 5 and 7.

1 mathematical form of g , which provides a weight equal to $(\Gamma/D)^2/\sigma$ to the
2 correction factor ξ , is chosen after an iterative procedure aiming at a smooth
3 distribution of experimental data. Data points in Figure 4.a are fitted by the
4 surface $G(\Gamma/D, v_i) = [v_1 + v_2 (\Gamma/D)^q] (v_3 + v_4 v_i^r)$, parametrized by coeffi-
5 cients $v_1 = -9.144 \cdot 10^{-2}$, $v_2 = 2.599$, $v_3 = 2.525$, $v_4 = 7.784 \cdot 10^{-1}$, $q = 1.757$,
6 $r = -5.831 \cdot 10^{-1}$, with root mean square residual equal to 0.054. Taking
7 into account the definition of g , the formulation of the bivariate function
8 $G(\Gamma/D, v_i)$ and the preliminary estimation obtained by BET in Eqs. (10)–
9 (12), it is $\xi \approx \sigma G/(\Gamma/D)^2$ and the corrected estimate, \hat{V}_{tip} , of tip speed is
10 finally written as:

$$\hat{V}_{tip}(v_i) = \xi V_{tip}^{BET} = \frac{k_{tip} \sigma}{(\Gamma/D)^2} [v_1 + v_2 (\Gamma/D)^q] (v_3 + v_4 v_i^r) v_i. \quad (14)$$

11 After characterizing the blade local flow condition, Eq. (4) is discussed
12 on an experimental basis. For each test, the figure of merit is calculated as

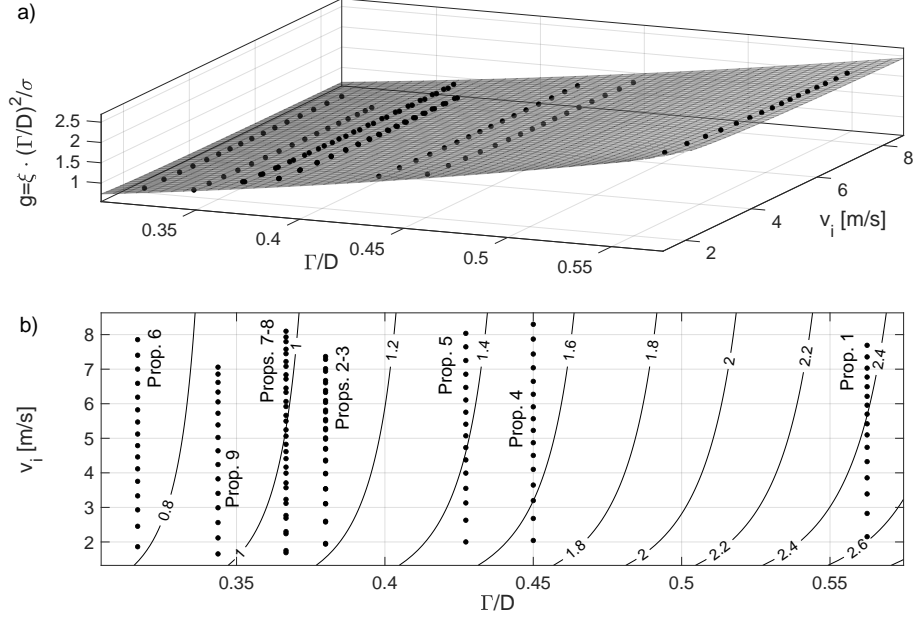


Figure 4: The non-dimensional function g for the complete set of propellers: a) measured data points and fitting surface; b) contour plot with corresponding iso-response lines.

$f = P_{id}/P_{sh}$, according to the definition given in Section 2, provided $P_{sh} =$
 $Q \Omega$ is derived from the product between the measured torque Q and the
angular rate Ω . Based on experimental results, the non-dimensional quantity
 $h \triangleq f \cdot (\Gamma/D)^\alpha$, defined in Section 3.1, is plotted in Figure 5 as a function of
 Γ/D and the Reynolds number Re , with the fitting parameters selected as
 $\alpha = -2$ and $\beta = 0$. Data points in Figure 5.a are fitted by a second-order
polynomial surface, represented by the bivariate function $H(\Gamma/D, Re) =$
 $f_{00} + f_{10}(\Gamma/D) + f_{01}Re + f_{20}(\Gamma/D)^2 + f_{11}(\Gamma/D)Re + f_{02}Re^2$, with coefficients
 $f_{00} = 17.03$, $f_{10} = -56.28$, $f_{20} = 50.61$, $f_{01} = 5.19 \cdot 10^{-5}$, $f_{11} = -6.034 \cdot 10^{-5}$,
 $f_{02} = -1.033 \cdot 10^{-10}$, and root mean square error residual equal to 0.072.
Taking into account the definition of h and the formulation adopted for
 $H(\Gamma/D, Re)$, it follows that the estimated figure of merit, \hat{f} , is expressed as

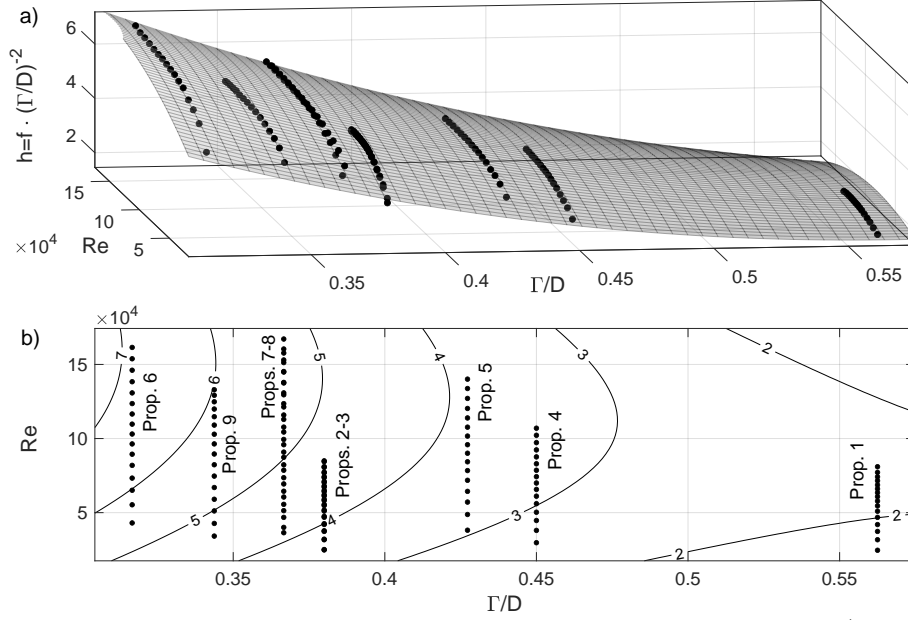


Figure 5: The non-dimensional function h for the complete set of propellers: a) measured data points and fitting surface; b) contour plot with corresponding iso-response lines.

1 a function of Reynolds number according to the model

$$\hat{f}(\text{Re}) = f_0 + f_1 \text{Re} + f_2 \text{Re}^2 \quad (15)$$

2 where

$$f_0 = (\Gamma/D)^2 [f_{00} + f_{10} (\Gamma/D) + f_{20} (\Gamma/D)^2] \quad (16)$$

$$f_1 = (\Gamma/D)^2 [f_{01} + f_{11} (\Gamma/D)] \quad (17)$$

$$f_2 = (\Gamma/D)^2 f_{02} \quad (18)$$

5 **Remark 1.** The results derived in terms of figure of merit characteriza-
6 tion and tip speed estimation are valid under Assumption 1, characterizing
7 a particular class of propellers. In what follows, the field of applicability
8 is discussed. First of all, commercial-off-the-shelf components are consid-
9 ered, optimized for multirotor vehicles. Then, the hobby and recreational

1 applications are excluded, where the use of very small propellers ($D < 8$
2 in, often tri/four-bladed) is widespread and determines high-agility racing
3 capabilities, thanks to the lower rotor inertia and small blade pitch angle.

4 With regard to professional applications, where the focus is posed on sta-
5 bility and endurance capabilities, it is interesting to note where the most im-
6 portant drone and propellers manufacturers targeted the market. In Table 2,
7 for example, the complete multicopter fleets of some of the main professional
8 drone companies are listed, with relevant data characterizing the maximum
9 take-off mass (MTOM) and the adopted propellers for 18 different products
10 [53, 54, 55]. The applications range from aerial photography and videography,
11 3D mapping, surveying, and environment monitoring, to precision farming
12 and crop spraying. Taking a look at the types of propellers, it can be noted
13 that 15 samples are characterized by $0.3 \leq \Gamma/D \leq 0.6$ and 9 of these have
14 a diameter $D < 16$. The result is that 50% of all the considered platforms
15 satisfy the requirements in Assumption 1 (the same percentage increases to
16 100% for multicopters with $MTOM \leq 6$ kg). In addition to the analysis of
17 existing vehicles, it is interesting to investigate how the spare market of mul-
18 ticopter components is structured, provided that the design of novel platforms
19 typically requires a wide spectrum of available propeller configurations.

20 To this aim, the complete catalogs of two of the biggest propellers manu-
21 facturers/resellers was dissected [56, 57]. In particular, a total of 89 propellers
22 was investigated, characterized by a different diameter, pitch, material, fin-
23 ish, and blade shape. Results are reported in Figure 6. It can be noted that
24 78% of propellers satisfies the constraint on rotor diameter ($D < 16$ in) while
25 93% complies with $0.3 \leq \Gamma/D \leq 0.6$. Summarizing, 71% of collected samples

Table 2: DJI, Freefly, and Yuneec multirotors with relevant data (the symbol 'F' in the fourth column is related to foldable blade configurations).

Multicopter	$MTOW$ [kg]	N	B	Γ [in]	D [in]	Γ/D
DJI						
Mavic Mini 2	0.242	4	2F	2.6	4.7	0.553
Mavic Air 2	0.570	4	2F	3.8	7.2	0.528
Mavic 2	0.906	4	2F	4.3	8.7	0.494
Phantom 4 PRO	1.388	4	2	5.5	9.4	0.585
Inspire 2	4.250	4	2	5	15	0.333
S800 EVO	8	6	2F	5.2	15	0.347
S1000	11	8	2F	5.2	15	0.347
Matrice 200 V2	6.140	4	2	6	17	0.353
Matrice 300 RTK	9	4	2F	10	21	0.476
Matrice 600 PRO	15.5	6	2F	7	21	0.333
MG-1P	24.5	8	2F	7	21	0.333
AGRAS T16	42	6	2F	9	33	0.273
AGRAS T20	47.5	6	2F	9	33	0.273
Freefly Systems						
Astro	8.382	4	2F	7	21	0.333
Alta-8	18.1	8	2F	6	18	0.333
Alta-X	34.86	4	2F	9	33	0.273
Yuneec						
Typhoon H520	1.633	6	2	5.7	9.8	0.582
Typhoon H3	2	6	2	5.7	9.8	0.582

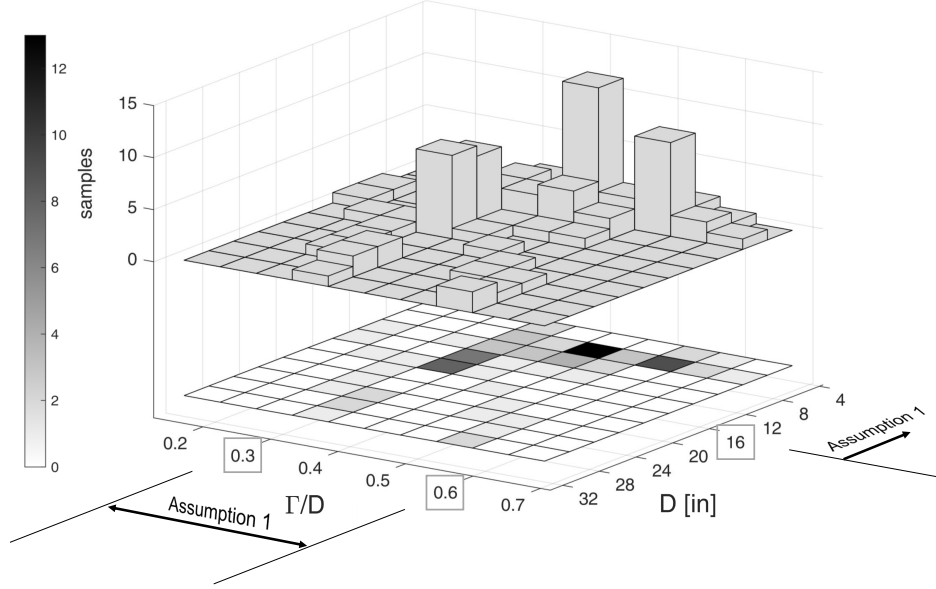


Figure 6: Bivariate histogram analysis of RC Timer and T-Motor propellers for professional multirotor applications.

1 falls under the requirements of Assumption 1.

2 It is thus shown that the proposed approach fits a wide applicability
3 range, provided that the considered class of propellers is a reference for cus-
4 tomized or off-the-shelf small-scale platforms. On the other hand, it must
5 be noted that such a market trend is also representative of all the cases where
6 high lifting capabilities are required but thrust is preferably distributed into
7 a higher number of smaller rotors. Despite the inherent increase of ideal
8 induced power, the adoption of such configurations is widespread and allows
9 1) the design of compact platforms, 2) the reduction of eventual damages
10 caused by blade impacts, 3) a higher degree of residual controllability after
11 failure of one or more propulsive units, and 4) reduced sensitivity to external
12 disturbances. In this respect, electrical and mechanical performance data for
13 a comprehensive range of motor and propeller combinations are reported in

1 [36], with a detailed statistical analysis.

2 4. Performance analysis and optimization

3 4.1. Hover endurance prediction

4 Consider the expression obtained in Eq. (3) and note that, for a multirotor
5 in a hovering condition, battery power is a constant. In Ref. [27] a novel
6 formulation for constant-power battery discharge process is proposed, where
7 discharge time is expressed as a function of discharged capacity and absorbed
8 power. Let $I = I(t)$ be the current provided by the battery pack at time t
9 and $C = C(t)$ be the discharged capacity, obtained as

$$C(t) = \int_0^t I(s) ds \quad (19)$$

10 Provided $P_b > 0$, the discharge process is stopped at time t_f when $C_f =$
11 $C(t_f) = K C_0$, with C_0 equal to the nominal battery capacity and $K < 1$
12 being a predefined discharge percentage. Discharge time is expressed in the
13 form

$$t_f = \delta P_b^\epsilon C_f^\beta \quad (20)$$

where coefficients $\delta > 0$, $\epsilon < -1$, and $0 < \beta < 1$, which depend on battery
technology, ambient temperature, and number of series-connected cells, are
determined experimentally. Conversely, when power is delivered by Li-Po
battery packs and no equipment is available to perform ad hoc battery tests,
the analytical results derived in [27] can be adopted, especially at a prelim-
inary design stage. In particular, let N_s be the number of series-connected
cells and define δ_0 , ϵ_0 , and β_0 as battery coefficients at the reference ambient

temperature, $\tau_0 = 23$ °C. It is:

$$\delta_0(N_s) = -0.1067 N_s^3 + 0.8960 N_s^2 + 2.488 N_s + 0.6299 \quad (21)$$

$$\epsilon_0(N_s) = 2.917 \cdot 10^{-4} N_s^3 - 1.375 \cdot 10^{-3} N_s^2 + 3.083 \cdot 10^{-3} N_s - 1.041 \quad (22)$$

1 while $\beta_0 = 0.9664$. In general, the parameters that define the variation of δ_0
2 and ϵ_0 as a function of N_s depend on battery technology and aging. With
3 this in mind, it is pointed out that the experiments at the base of Eqs. (21)
4 and (22) were performed on battery packs with exactly the same technology,
5 at approximately half of their operational lifespan, as a compromise between
6 better performance (when the battery pack is new) and degraded conditions.
7 Of course, an accurate estimate of discharge time would require to repeat
8 the whole experimental campaign at various stages of battery life, in order
9 to estimate the updated parameters and the effective capacity as battery
10 aging and degradation develop. This can be performed according to the
11 procedure in [27] by means of an electronic load or by collecting flight data
12 in terms of both hour-integral discharged capacity and delivered power, for
13 different loading conditions. Anyway, to the authors' experience with Li-Po
14 batteries, the trends of $\delta_0(N_s)$ and $\epsilon_0(N_s)$ are correctly evaluated, with only
15 minor variations.

In Ref. [27] an experiment was also conducted to investigate the effect of environment temperature on battery performance. In the present framework, the analyzed trend is extrapolated by assuming a linear regression, based on the available experimental data respectively obtained at 23 °C and at a lower temperature, namely 17 °C. Provided $\Delta\tau = \tau - \tau_0$ is the temperature variation with respect to the reference case, the environment-compensated

battery parameters are expressed as a function of N_s and $\Delta\tau$ as

$$\delta(N_s, \Delta\tau) = \delta_0(N_s) (1 - c_1 \Delta\tau) \quad (23)$$

$$\epsilon(N_s, \Delta\tau) = \epsilon_0(N_s) (1 - c_2 \Delta\tau) \quad (24)$$

$$\beta(\Delta\tau) = \beta_0 (1 - c_3 \Delta\tau) \quad (25)$$

- 1 where $c_1 = 0.0046 \text{ 1/}^\circ\text{C}$, $c_2 = 0.0024 \text{ 1/}^\circ\text{C}$, and $c_3 = 0.0011 \text{ 1/}^\circ\text{C}$ are correc-
2 tion coefficients.

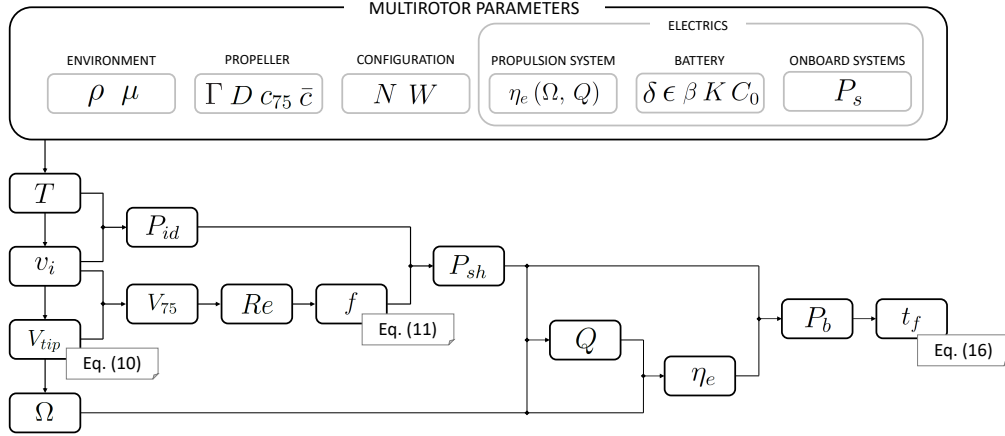


Figure 7: The proposed procedure to estimate battery power and flight time for a multirotor at hover.

- 3 In Figure 7 the complete procedure necessary to estimate the hovering
4 flight time for a given multirotor configuration is detailed. The set of pa-
5 rameters that are required to be measured or estimated a priori are reported
6 at the top of the same figure. For a given take-off weight and multirotor
7 configuration, the required thrust T of the single rotor is used to derive the
8 induced speed v_i and the corresponding ideal induced power P_{id} . By Eq. (14)
9 one estimates the corrected blade tip speed and the Reynolds number at 75%
10 blade radius, such that the figure of merit can be calculated according to the

1 experimental model in Eqs. (15)–(18). Given the ideal power P_{id} , corrected
2 by the figure of merit to the shaft power P_{sh} , it is possible to characterize
3 the torque $Q = P_{sh}/\Omega$ applied by the electric motor to its rotor and the
4 efficiency η_e of the electric propulsion system at that operating point. As
5 a final step, the total battery power is derived as in Eq. (3), provided the
6 power necessary for onboard systems P_s is known. The hovering time follows
7 from Eq. (20) for a prescribed percentage of the nominal battery capacity
8 C_0 , in the considered environmental conditions.

9 *4.2. Sizing of battery capacity*

10 In this section, the optimal value of the battery capacity that maximizes
11 hover endurance is determined, following an approach similar to that de-
12 scribed in [20], where the optimal battery pack configuration was obtained
13 by using the classical Peukert discharge model. For the aim of the present
14 analysis, the total take-off weight is conveniently decomposed into

$$W = W_b + W_0 \quad (26)$$

15 where W_b is the battery weight and W_0 is the operative empty weight made
16 of contributions from: a) the frame (structure and rigging), b) the propul-
17 sive system (motors, electronic speed controllers, and propellers), c) the
18 avionics (autopilot and communication system), and d) the eventual payload
19 equipments. Let $\chi = W_b/E_0 = W_b/(\mathcal{V}_0 C_0)$ indicate the nominal battery
20 weight/energy ratio (that is, the inverse of battery energy density), such
21 that the aircraft total weight in Eq. (26) can be rewritten as

$$W = W_0 + \chi \mathcal{V}_0 C_0 \quad (27)$$

1 where \mathcal{V}_0 is battery nominal voltage. Rotorcraft sizing is thus performed
2 assuming take-off weight W as the independent variable in Eqs. (3) and
3 (14), and determining battery capacity from Eq. (27),

$$C_0 = \frac{W - W_0}{\chi \mathcal{V}_0} \quad (28)$$

4 Given a predefined discharge percentage $K \leq 1$, flight endurance is thus
5 estimated according to Eq. (20) as a function of take-off weight W and,
6 hence, of rated capacity C_0 .

7 The necessary condition for the optimal value of W which maximizes
8 the hovering flight time t_f (that is, the best endurance weight configuration,
9 $W = W_{be}$) is obtained by solving the equation $dt_f/dW = 0$. The sign
10 of the first derivative before and after its zeros (or, equivalently, the sign
11 of the second derivative at the zeros) allows for identifying maxima and
12 minima of the endurance curve. Despite the analytical formulation derived
13 in Section 3 for the figure of merit characterization, it is clear that, in the most
14 general case, the propulsive system efficiency η_e is a function of the estimated
15 rotor angular rate Ω and applied torque Q , which is estimated from vehicle
16 datasheet or determined experimentally. Hence, an analytical solution for
17 the equation $dt_f/dW = 0$ (and the sign of d^2t_f/dW^2) with general validity is
18 not available. An iterative root search algorithm, such as Newton–Raphson
19 scheme [58], needs to be implemented and the second derivative at the zero
20 can be evaluated by means of centered differences. As an alternative, the
21 function that relates W to the expected performance in Eq. (20) can be
22 plotted and the best weight configuration identified either graphically on the
23 plot or numerically by means of a search algorithm, such as the parabolic
24 search or the simplex method [59].

1 An approximate closed-form solution, W_{be}^* , to the optimal sizing problem
 2 can be made available on the basis of the following simplifying assumptions:
 3 1) η_e is a constant; 2) the power required for avionics and payload is negligible
 4 with respect to the power delivered to the propulsion system, namely $P_s \ll$
 5 $N P_{sh}$; 3) the required blade tip speed is simply estimated on the basis of
 6 BET according to Eq. (10), where $V_{tip}^{BET} = k_{tip} v_i$, with no correction; 4) the
 7 effect of induced flow on local blade airspeed computation is disregarded, that
 8 is to say $v_i \ll 0.75 \cdot V_{tip}$ and $V_{75} \approx 0.75 \cdot V_{tip}$; 5) an ideal battery is considered
 9 where discharge time is obtained by Eq. (20) with $\epsilon = -1$ and $\beta = 1$. Taking
 10 into account the assumptions given above, the expression dt_f/dW results to
 11 be proportional to a fourth order polynomial and $dt_f/dW = 0$ if

$$q_0 + q_1 y + q_2 y^2 + q_4 y^4 = 0 \quad (29)$$

where $y = \sqrt{W}$ and

$$q_0 = 96 \mu^2 f_0 A N W_0 \quad (30)$$

$$q_1 = 24 \mu c_{75} f_1 k_{tip} W_0 \sqrt{2 \rho A N} \quad (31)$$

$$q_2 = 9 c_{75}^2 f_2 k_{tip}^2 W_0 - 32 \mu^2 f_0 A N \quad (32)$$

$$q_4 = 9 c_{75}^2 f_2 k_{tip}^2 \quad (33)$$

12 are constant coefficients. Based on Eqs. (16)–(18), it is $f_0, f_1 > 0$ and $f_2 < 0$
 13 for all propellers selected under Assumption 1, with the result that $q_0 > 0$,
 14 $q_1 > 0$, $q_2 < 0$, and $q_4 < 0$. The sequence of signs in Eq. (29) is thus $++--$,
 15 which indicates that, according to Descartes' rule [60], there is only one real
 16 positive solution, in the form:

$$W_{be}^* = y_{be}^{*2} = \left(S + \frac{1}{2} \sqrt{-4 S^2 - \frac{2 q_2}{q_4} - \frac{q_1}{q_4 S}} \right)^2 \quad (34)$$

where

$$S = \frac{1}{2} \sqrt{-\frac{2q_2}{3q_4} + \frac{1}{3q_4} \left(Q + \frac{\Delta_0}{Q} \right)} \quad (35)$$

$$Q = \sqrt[3]{\frac{\Delta_1 + \sqrt{\Delta_1^2 - 4\Delta_0^3}}{2}} \quad (36)$$

$$\Delta_0 = q_2^2 + 12q_4q_0 \quad (37)$$

$$\Delta_1 = 2q_2^3 + 27q_4q_1^2 - 72q_4q_2q_0 \quad (38)$$

1 Provided that the polynomial in Eq. (29) grows towards $-\infty$ as $y \rightarrow +\infty$,
 2 the first derivative is expected to be positive before the root and negative
 3 after it, thus indicating that the zero of the first derivative corresponds to
 4 a maximum for t_f . Finally, the optimal value of the battery capacity that
 5 maximizes hover endurance is obtained from Eq. (28) with $W = W_{be}^*$.

6 5. Results

7 The proposed technique, developed to estimate the hovering performance
 8 of multirotor platforms and to provide battery-sizing guidelines, is numer-
 9 ically validated. In particular, a comparison is provided between model-
 10 predicted data and the results of flight tests, in terms of required battery
 11 power and hovering endurance. Flight data are provided by the rotorcraft
 12 manufacturers (see configurations MR1, MR2, and MR3) or are obtained
 13 from a dedicated experimental campaign, performed by the authors at the
 14 University of Bologna premises (platforms MR4 and following).

15 5.1. Battery power prediction

16 In the present section, four different existing platforms are analyzed (re-
 17 spectively named *MR1*, *MR2*, *MR3*, and *MR4*), with MTOM ranging from

about 1.3 to 25 kg and propeller diameter from 9 to 21 in. Battery power is predicted according to the proposed approach and compared with the results of flight data. Main results are then summarized in Table 3.

5.1.1. MR1: DJI Spreading Wings S1000

The DJI Spreading Wings S1000 is characterized by $N = 8$ rotors, each provided with a two-bladed folding CF propeller with $D = 15$ in and $\Gamma = 5.2$ in. Dihedral and tilt angles are, respectively, $\psi = 8$ deg and $\phi = 3$ deg, provided the same nomenclature and definitions of [6] are adopted. Power is delivered by a Li-Po battery pack with $N_s = 6$ series-connected Li-Po cells, through an integrated system made by a proprietary 40 A ESC and a 4114-PRO brushless electric motor with speed constant $k_v = 400$ rpm/V. With a take-off mass $m = 9.5$ kg, the total battery power as measured by the manufacturer is equal to 1 500 W [53].

In the given configuration, the thrust required by the single rotor is $T = W / (N \cos \psi \cos \phi) = 11.78$ N, which produces an induced flow with speed $v_i = 6.49$ m/s and rotor ideal power $P_{id} = 76.5$ W, assuming sea-level standard atmospheric conditions ($\tau = 15$ °C, $\rho = 1.225$ kg/m³, and $\mu = 1.789 \cdot 10^{-5}$ Pa s). Provided $\bar{c} = 0.0175$ m, the considered propeller is characterized by solidity $\sigma = 0.0586$ while the nominal pitch angle at 75% radius is $\theta_{75} = 0.1461$ rad, according to Eq. (12). Based on BET analysis, the estimated blade tip speed in Eq. (10) is $V_{tip}^{BET} = 135.85$ m/s, with $k_{tip} = 20.92$. Given $\Gamma/D = 0.347$, the corrected tip speed by Eq. (14) is $\hat{V}_{tip} = 57.75$ m/s (corresponding to $\Omega = 303.2$ rad/s). At the considered operating point it is $V_{75} = 43.80$ m/s (which approximately equals the quantity $0.75 \cdot \hat{V}_{tip} = 43.31$ m/s) and the Reynolds number is $Re = 56\,980$, provided

$c_{75} = 0.019$ m is the local chord length. The figure of merit is estimated from the model in Eq. (15) as $f = 0.605$, provided the coefficients in Eqs. (16)–(18) are $f_0 = 0.4329$, $f_1 = 3.726 \cdot 10^{-6}$, and $f_2 = -1.241 \cdot 10^{-11}$. The single rotor shaft power is thus $P_{sh} = P_{id}/f = 126.4$ W, the total power required to hover is $P_h = N P_{sh} = 1010.9$ W, and the torque applied to the propeller by the electric motor is $Q = P_{sh}/\Omega = 0.417$ Nm. Assuming no payload is powered by the main battery pack, the only contribution to P_s is provided by the avionics. Based on the statistical analysis performed in [61] on DJI products, it is assumed $P_s = 5$ W, which accounts for the current absorbed by the onboard computer and the electric driving system, when no thrust is generated. The electric propulsion system is characterized by DriveCalc online computation tools [48]. In particular, the system made of the considered ESC and motor is outlined from the available component database and the overall electric efficiency is evaluated exactly at the given operating point, where $\eta_e = 0.68$. Taking into account Eq. (3), the total power requested from the battery for the hovering flight is $P_b = 1492.3$ W, with an estimation error $\varepsilon_P = -0.51\%$ with respect to the nominal value.

5.1.2. MR2: DJI AGRAS MG-1P

The procedure described above is applied to another professional platform for which DJI provides some flight data, namely the AGRAS MG-1P, engineered for agricultural spraying activities. The platform has $N = 8$ rotors, each provided with a two-bladed folding CF propeller with $D = 21$ in, $\Gamma = 7$ in, $\bar{c} = 0.029$ m, and $c_{75} = 0.021$ m (configuration not compliant to Assumption 1). The rotor configuration is planar, except for the tilt angle $\phi = 3$ deg, and thrust is provided by an integrated DJI system made of a 25 A ESC

1 and a 6010 brushless electric motor. Energy is delivered by a MG-12000P
2 Li-Po Intelligent Flight Battery with nominal voltage $\mathcal{V}_0 = 44.4$ V ($N_s = 6$)
3 and capacity $C_0 = 12$ Ah. The total electric power measured during a stable
4 hovering condition is 3 250 W when the take-off mass is $m = 22.5$ kg [53].

5 In the same condition, the predicted shaft power required to hover is
6 $P_{sh} = 309.0$ W, with the figure of merit being $f = 0.635$, and the torque
7 is $Q = 1.16$ Nm. The overall electric efficiency at the considered operating
8 point is retrieved from the curves provided by the manufacturer in [62] and
9 is equal to $\eta_e = 0.81$. With respect to the systems power consumption, some
10 optimistic data are reported in [32], where avionics (10 W) and payload (40
11 W) are taken into account for a non-specified spraying mode of pesticides and
12 fertilizers. Taking into account the presence of the onboard high precision
13 radar module (12 W), it follows $P_s = 62$ W and the total power requested
14 from the battery is $P_b = 3\,114.3$ W, with a prediction error equal to -4.18% .

15 5.1.3. MR3: DJI Phantom 4 V2.0

16 A small rotorcraft, identified as a study case in [63], is analyzed with
17 characteristics similar to the DJI Phantom 4 V2.0 (reference drone). The
18 platform has $N = 4$ rotors with two-bladed 9×4.5 E APC propellers ($D = 9$
19 in, $\Gamma = 4.5$ in, $\bar{c} = 0.019$ m, $c_{75} = 0.022$ m), designed for fixed-wing electric
20 aircraft (thus partially disregarding Assumption 1). Dihedral and tilt angles,
21 not specified in [63], are assumed to be equal to the reference drone, for which
22 $\psi = 8$ deg and $\phi = 3$. Power is delivered by a Li-Po battery with nominal
23 voltage $\mathcal{V}_0 = 14.8$ V ($N_s = 4$) and capacity $C_0 = 5.9$ Ah. Propulsion is
24 obtained by a set of 12 A ESCs and Flyduino X2208 brushless motors. With
25 a take-off mass $m = 1.375$ kg, each ESC requires 39 W of electrical power

1 at hover, the torque delivered by the electric motor to its propeller is 0.05
2 Nm at 5 600 rpm, and the shaft power is equal to 31 W. Assuming $P_s = 5$ W
3 [61], the total battery power is thus $(39 \cdot 4) + 5 = 161$ W, according to [63].

4 Given $\Gamma/D = 0.5$ and $\sigma = 0.106$, the estimated rotor angular rate is
5 $\Omega = 554.8$ rad/s (5 298 rpm), with an error equal to -5.39% with respect
6 to the indicated value. A figure of merit $f = 0.644$ is determined, and the
7 predicted shaft power is $P_{sh} = 30.8$ W (estimation error: -0.65%). The
8 torque results to be $Q = 0.056$ Nm (estimation error: $+11.2\%$) and, based
9 on the efficiency curves provided by the authors in [63], the propulsion system
10 is characterized by $\eta_e = 0.79$. The required electrical power for each ESC is
11 38.9 W (estimation error: -0.26%) and the total power requested from the
12 battery for the hovering flight is $P_b = 160.5$ W (estimation error: -0.31%).

13 5.1.4. MR4: DJI Spreading Wings S800 EVO

14 The proposed method is also validated by means of flight tests performed
15 by the authors at the University of Bologna premises. A DJI Spreading
16 Wings S800 EVO is considered, characterized by $N = 6$ rotors and the same
17 propulsion system analyzed for the DJI S1000 in Section 5.1.1. Dihedral
18 and tilt angles are, respectively, $\psi = 8$ deg and $\phi = 3$ deg and power is
19 delivered by a Tattu 25C battery made of $N_s = 6$ series-connected Li-Po
20 cells with nominal voltage $\mathcal{V}_0 = 22.2$ V and capacity $C_0 = 22$ Ah. The empty
21 operative mass is 4 kg and the considered battery weighs 2.509 kg, such that
22 the take off mass is $m = 6.509$ kg and the thrust required from the single
23 rotor is $T = 10.76$ N. A hovering flight test was performed at the ambient
24 temperature $\tau = 15$ °C and pressure $p = 98\,460$ Pa, with estimated air
25 density $\rho = 1.1904$ kg/m³ and dynamic viscosity $\mu = 1.789 \cdot 10^{-5}$ Pa.s. Taking

Table 3: Analyzed multirotor platforms and battery power prediction errors.

Multirotor	Mass [kg]	N	D [in]	Γ [in]	f	η_e	P_b est. [W]	P_b meas. [W]	ε_P [%]
MR1	9.5	8	15	5.2	0.605	0.68	1 492.3	1 500	-0.51
MR2	22.5	8	21	7	0.635	0.81	3 114.3.3	3 250	-4.18
MR3	1.375	4	9	4.5	0.644	0.79	160.5	161	-0.31
MR4	6.509	6	15	5.2	0.597	0.85	833.4	828.2	0.63

into account the information obtained in flight by averaging the readings of a wattmeter sensor, the measured power resulted to be 828.2 W.

According to the proposed prediction method, the shaft power required to hover is $P_{sh} = 113.4$ W and the torque is $Q = 0.39$ Nm, with the figure of merit being $f = 0.597$. The electric propulsion system is characterized by DriveCalc online computation tool [48], according to which $\eta_e = 0.85$. The only contribution to P_s is provided by the avionics, made of the onboard computer and telemetry system. Based on the statistical analysis performed in [61], it is assumed $P_s = 5$ W and the estimated total power delivered by the battery pack is $P_b = 833.4$ W. In this case, the error of the proposed technique for predicting battery power is only +0.63% with respect to obtained measurement.

5.2. Flight endurance and sizing procedure validation

In what follows, two test cases are analyzed. While addressing the validity of the battery power estimation method, endurance tests allow to address the flight time prediction problem presented in Section 4.

5.2.1. MR5: UNIBO MDV-X4 Multirotor

The first case is represented by the analysis of a rotorcraft with $N = 4$ planar rotors, developed at the University of Bologna (platform MR5, see



Figure 8: The quadcopter MDV-X4 developed at the University of Bologna (MR5).

1 Figure 8). Power is delivered by the parallel connection of 2 Tattu 25C Li-
 2 Po batteries with the same specifications reported in Section 5.1.4, such that
 3 $\mathcal{V}_0 = 22.2$ V, and the nominal capacity is $C_0 = 22 \cdot 2 = 44$ Ah. Propulsion is
 4 obtained by a set of T-Motor U8 motors with $k_v = 135$ rpm/V [64], driven
 5 by T60A electronic controllers, and CF propellers by T-Motor with $D = 29$
 6 in, $\Gamma = 9.5$ in, $\bar{c} = 0.057$ m, and $c_{75} = 0.055$ m (configuration not compliant
 7 to Assumption 1). The empty operative mass is 4.245 kg and the considered
 8 battery pack weighs $2.509 \cdot 2 = 5.018$ kg, with the result that the take off mass
 9 is $m = 9.263$ kg and the thrust required from the single rotor is $T = 22.71$
 10 N. Three hovering flight tests were performed at the ambient temperature
 11 $\tau = 22$ °C and pressure $p = 98\,650$ Pa, with estimated air density $\rho = 1.1644$
 12 kg/m³ and dynamic viscosity $\mu = 1.822 \cdot 10^{-5}$ Pa s. During each flight, the
 13 battery pack was discharged to the 80% of nominal capacity, that is to say
 14 $C_f = K C_0 = 0.8 \cdot 44 = 35.2$ Ah, starting from an initial fully-charged

condition. The average values of the measured battery power P_b and flight time t_f resulted to be 703.7 W and 60.4 min, respectively.

Based on the available data, the predicted rotor angular rate is $\Omega = 171.4$ rad/s. The shaft power required to hover is $P_{sh} = 154.4$ W, with the figure of merit being $f = 0.7$ at $\text{Re} = 154\,853$. The efficiency of the electric propulsion system is retrieved from [47], where $\eta_e = 0.88$. No power-consuming payload is carried on board and the avionics is represented by a DJI Wookong-M system, for which $P_s = 5$ W. The predicted power required from the battery pack is $P_b = 707.1$ W (estimation error: +0.48%). Hovering endurance is estimated by Eq. (20), where $\delta = 25.07$, $\epsilon = -1.011$, and $\beta = 0.9675$ are the temperature-compensated battery coefficients, obtained from Eqs. (21)–(25). Predicted flight time is 61.3 min, with an estimation error of +1.49%.

5.2.2. MR6/7/8/9: DJI F550 Flame Wheel

The battery-sizing procedure described in Section 4.2 is experimentally investigated for a DJI F550 Flame Wheel planar hexarotor ($N = 6$), where propulsion is provided by a set of DJI Opto 30A ESCs and DJI 2212 brushless motors. The nominal empty operative mass is 1.35 kg, which includes the contribution of computer and telemetry system, based on a Pixhawk PX4 board with power absorption $P_s = 5$ W. In order to calculate the battery weight/energy ratio to be used during the design process, a reference 25C Li-Po battery by Tattu is considered with nominal voltage $\mathcal{V}_0 = 14.8$ V ($N_s = 4$), capacity $C_0 = 9$ Ah, and mass 0.810 kg ($W_b = 7.94$ N), with the result that $\chi = W_b / (\mathcal{V}_0 C_0) = 0.0596$ N/(Wh).

The propulsion system made of ESC and motor was previously characterized over an adequate range of angular rate and torque by the RCbenchmark

1 thrust stand at room temperature $\tau = 24$ °C, with voltage stabilized at 14.8
2 V. Adopting the same procedure described in Section 3, static thrust tests
3 were thus performed on three sample propellers (the same marked as 1, 2,
4 and 4 in Table 1) and the data relative to the measured torque, angular
5 rate, and electrical power were collected. Provided that the electrical effi-
6 ciency is calculated as the ratio between the available shaft power and the
absorbed electrical power, obtained results are reported in Figure 9. Data

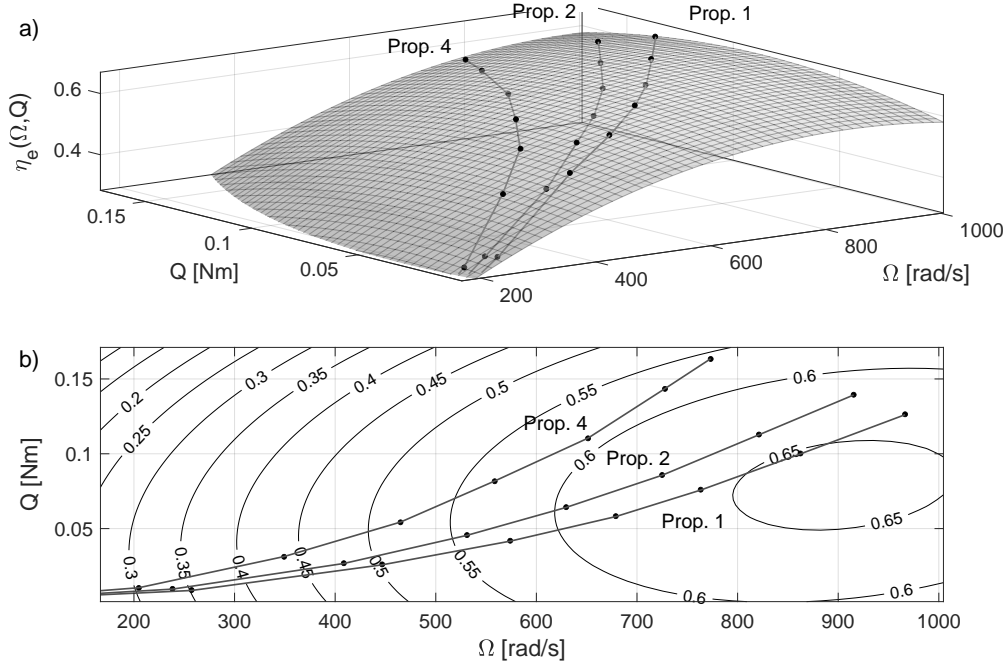


Figure 9: Electrical efficiency of a DJI 2212 brushless motor with DJI Opto 30A ESC: a) measured data points and fitting surface; b) contour plot with corresponding iso-response lines.

7
8 points in Figure 9.a are fitted by a second-order polynomial surface, such
9 that $\eta_e(\Omega, Q) = p_{00} + p_{10}\Omega + p_{01}Q + p_{20}\Omega^2 + p_{11}\Omega Q + p_{02}Q^2$, with coeffi-
10 cients $p_{00} = 7.145 \cdot 10^{-2}$, $p_{10} = 1.259 \cdot 10^{-3}$, $p_{01} = 0.4377$, $p_{20} = -7.513 \cdot 10^{-7}$,
11 $p_{11} = 1.284 \cdot 10^{-3}$, $p_{02} = -10.13$, and root mean square residual equal to

Table 4: Predicted and measured performance data for different DJI F550 configurations equipped with the same battery pack (Li-Po, $N_s = 4$, $C_0 = 9$ Ah, $K = 0.6$).

Configuration	W_0 [N]	Propeller	f	η_e	P_b est. [W]	P_b meas. [W]	ε_P [%]	t_f est. [min]	t_f meas. [min]	ε_t [%]
MR6-9	18.51	1	0.683	0.646	468.2	459.3	1.94	10.03	9.83	2.03
MR7-9	13.24	1	0.676	0.625	351.4	352.3	-0.26	13.45	13.05	3.07
MR8-9	18.86	4	0.668	0.584	432.2	426.0	1.46	10.88	10.77	1.02
MR9-9	13.59	4	0.654	0.557	334.5	342.2	-2.26	14.15	14.13	0.14

1 0.015.

2 Starting from the reference platform described above, 4 different multi-
3 rotor configurations are defined, which differ by the selection of propellers
4 (the ones marked as 1 and 4 in Table 1) and the particular empty-operative
5 weight W_0 (varied by the quantity $\Delta W_0|_{pl} = 5.27$ N through the equipment
6 of an additional 0.537 kg payload system). For each configuration, a flight
7 test was performed at temperature $\tau = 26$ °C and pressure $p = 97\,903$ Pa (es-
8 timated air density $\rho = 1.1401$ kg/m³ and dynamic viscosity $\mu = 1.841 \cdot 10^{-5}$
9 Pas) while discharging the battery to the 60% of nominal capacity ($C_f =$
10 $K C_0 = 0.6 \cdot 9 = 5.4$ Ah). Main results are reported in Table 4 in terms of
11 model-predicted figure of merit, electrical efficiency, battery power, and flight
12 endurance. To this end, battery coefficients, evaluated from Eqs. (21)–(25),
13 are $\delta = 17.93$, $\epsilon = -1.025$, and $\beta = 0.9632$. Data are compared to measured
14 values and estimation errors are calculated. Note that, in the same loading
15 condition, the adoption of Propellers '4' determines a total increase of empty
16 weight by about $\Delta W_0|_{prop} = 0.35$ N with respect to the case in which pro-
17 pellers '1' are adopted. It is evident from Table 4 that, for all the analyzed
18 configurations, the estimation errors of both battery power (ε_P) and flight
19 time (ε_t) are lower than 5%, which vindicates the validity of the proposed
20 approach.

In Figure 10 the discussion of the sizing procedure illustrated in Section 4.2 is applied to the present case, while comprising the data points already reported in Table 4 (round markers). In particular, the curves representing predicted endurance are plotted as a function of nominal capacity for all the considered configurations. The presence of a maximum in all the

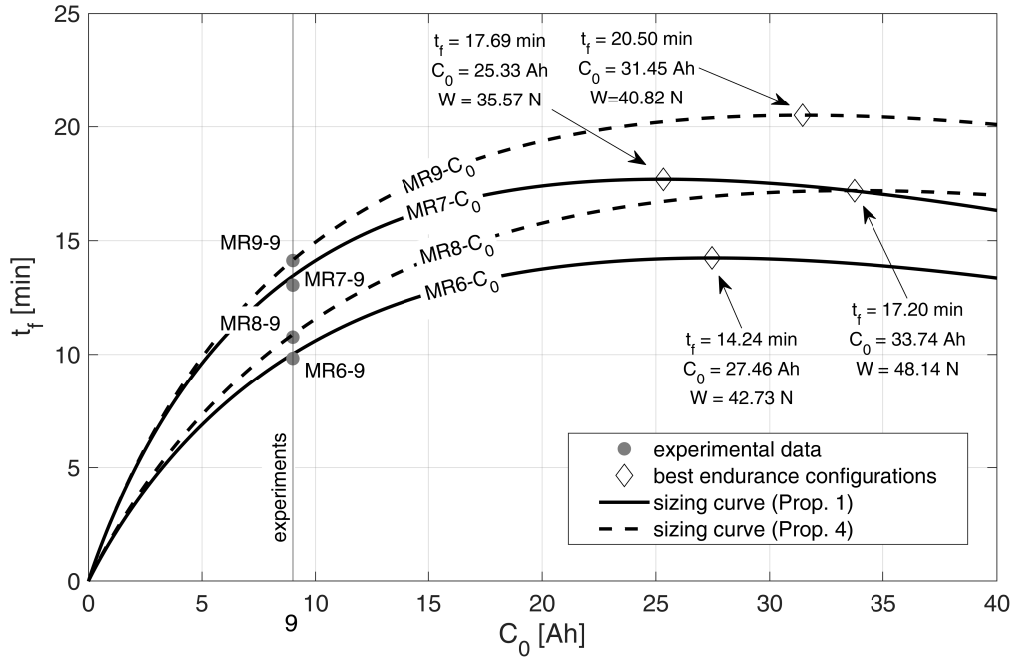


Figure 10: Predicted and measured performance data for different DJI F550 configurations (the symbol 'MRX-Y' refers to multirotor configuration 'X' with battery nominal capacity 'Y' Ah).

curves clearly points out that, if endurance is pursued as the most relevant goal in the design process, it is useless to increase the size of the battery pack beyond a certain limit, provided that the corresponding growth in rotorcraft weight affects required power. Best endurance configurations are indicated in Fig. 10 by diamond markers. Note that, for all the considered configurations, the maximum is 'flat', meaning that very large variations of battery

weight are necessary for marginal gains in terms of expected flight time. From the practical standpoint, this growth in battery capacity is clearly not justified, when one considers that a bigger battery is more expensive and the corresponding additional weight typically requires more powerful motors and robust structures.

As an example, consider configuration *MR6* – 9 in Fig. 10, for which the predicted hover endurance is 10.03 min when $K = 0.6$. Assume that, in order to comply with more stringent requirements, the endurance must be extended by 2 minutes with the same discharge percentage. Taking into account Figure 10, the target flight time of 12.03 min can be obtained in 2 ways. In the first case, the same set of propellers is used (Propellers 1) but a bigger battery with nominal capacity equal to at least 13.09 Ah is required (corresponding take-off weight: $W = 30.75$ N). In the second case, the multicopter is equipped with Propellers 4 and a bigger battery with at least 10.72 Ah (take-off weight: $W = 28.32$ N). At the time of writing the present paper, the considered battery type by Tattu is characterized by a cost of about 15.60 US dollars per Ah [65]. The complete sets of Propellers 1 and 4, equivalent to the DJI product, respectively cost 4.50 and 7.50 dollars, according to [56]. With this in mind, the first upgrade solution would determine an additional cost of $4.09 \cdot 15.60 = 63.80$ dollars (battery upgrade). The second solution would require 29.83 dollars, of which $1.72 \cdot 15.60 = 26.83$ dollars for the battery upgrade and only 3 dollars for the replacement of the full propellers set.

The model derived in Eqs. (34)–(38), which analytically provides an approximate value to the best endurance capacity, is finally validated. The

1 exact best endurance configurations are detailed in Figure 10. The minimum
 2 estimation error is obtained for platform $MR9 - C_0$, where $W_{be} = 40.82$ N
 3 and $W_{be}^* = 41.96$ N, and is equal to +2.79%. The maximum error is obtained
 4 for platform $MR8 - C_0$, where $W_{be} = 48.14$ N and $W_{be}^* = 54.36$ N, and is
 5 equal to +12.92%.

6 **6. Conclusions**

7 Performance of an electrically-powered multirotor is discussed by means
 8 of a novel integral formulation for constant-power battery-discharge process.
 9 The analysis is based on the estimation of power required from the battery
 10 pack during a hovering condition. Starting from the results available from
 11 blade element theory, an analytical expression is derived, on an experimental
 12 basis, for the figure of merit of a class of commercial-off-the-shelf propellers.
 13 The main outcome from these propeller tests is discussed, provided that the
 14 blade Reynolds number plays a significant part in determining its perfor-
 15 mance. As a by-product, the trim angular rate of the rotors and the torque
 16 applied by the electric motors to the propellers are derived.

17 Numerical simulations and an experimental campaign validate the capa-
 18 bility of the proposed approach to accurately predict the hover endurance of
 19 existing platforms. At the same time, a very simple procedure is outlined
 20 to design novel configurations or upgrade a selected propulsion system, in
 21 order to satisfy given requirements in terms of flight time, take-off weight,
 22 and prototyping costs. In this respect, a closed-form solution to the best
 23 endurance battery capacity is also derived. The effectiveness of the proposed
 24 approach and the simplicity of the analytical formulation are shown to be of

1 general validity and prove to be encouraging in the framework of rotorcraft
2 preliminary sizing.

3 Future developments, allowing for improved performance prediction and
4 optimal sizing procedures include: 1) detailed characterization of the induced
5 flow by the propeller in order to further investigate the contribution of both
6 induced and profile power; 2) the extension of the applicability field of the
7 proposed method to a wider family of commercial-of-the-shelf propellers,
8 including counter-rotating configurations, thus relaxing the requirements of
9 Assumption 1; 3) the derivation of estimation algorithms to perform battery
10 parameter identification in-flight; 4) the adaptation of the proposed method
11 to the analysis of different flight conditions, such as cruise, climb, or descent,
12 with the aim to accurately estimate the required power, endurance, and range
13 performance, and to provide sizing guidelines for complex mission scenarios.

14 **References**

- 15 [1] S. Harwey, A. Lucieer, Assessing the Accuracy of Georeferenced Point
16 Clouds Produced via Multi-View Stereopsis from Unmanned Aerial Ve-
17 hicle (UAV) Imagery, *J. Remote Sensing*, Vol. 4, No. 6, 2012, 1573–1599,
18 doi: 10.3390/rs4061573
- 19 [2] G. Cai, J. Dias, L. Seneviratne, A Survey of Small-Scale Unmanned
20 Aerial Vehicles: Recent Advances and Future Development Trends,
21 *Unmanned Systems*, Vol. 2, No. 2, 2014, 175–199, doi: 10.1142/
22 S2301385014300017
- 23 [3] E.L. de Angelis, F. Giuliotti, G. Rossetti, Multicopter aircraft formation

- 1 flight control with collision avoidance capability, *Aerosp. Sci. Technol.*,
2 Vol. 77, June 2018, 733–741, doi: 10.1016/j.ast.2018.04.002
- 3 [4] K. Valavanis, G.J. Vachtsevanos, *Handbook of Unmanned Aerial Vehi-*
4 *cles*, Springer Reference Vol. 1, Netherlands, 2015, 308–309.
- 5 [5] E.L. de Angelis, et al., Optimal autonomous multirotor motion planning
6 in an obstructed environment, *Aerosp. Sci. Technol.*, Vol. 87, April 2019,
7 379–388, doi: 10.1016/j.ast.2019.03.017
- 8 [6] E.L. de Angelis, Stability analysis of a multirotor vehicle hovering
9 condition, *Aerosp. Sci. Technol.*, Vol. 72, Jan. 2018, 248–255, doi:
10 10.1016/j.ast.2017.11.017
- 11 [7] Z. Zhang, J. Li, J. Wang, J., Sequential convex programming for non-
12 linear optimal control problems in UAV path planning, *Aerosp. Sci.*
13 *Technol.*, Vol. 76, May 2018, 280–290, doi: 10.1016/j.ast.2018.01.040
- 14 [8] M.H. Hwang, H.R. Cha, S.Y. Jung, Practical Endurance Estimation for
15 Minimizing Energy Consumption of Multirotor Unmanned Aerial Vehi-
16 cles, *Energies*, Vol. 11, No. 9, Aug. 2018, 1–11, doi: 10.3390/en11092221
- 17 [9] Z. Xunfei, et al., Cycle life estimation of lithium–ion polymer batteries
18 using artificial neural network and support vector machine with time–
19 resolved thermography, *Microelectron. Reliab.*, Vol. 79, 2017, 48–58, doi:
20 10.1016/j.microrel.2017.10.013
- 21 [10] X. Hu, D. Cao, B. Egardt, Condition monitoring in advanced battery
22 management systems: moving horizon estimation using a reduced elec-

- 1 trochemical model, IEEE ASME Trans. Mechatron., Vol. 23, No. 1,
2 2017, 167–178, doi: 10.1109/TMECH.2017.2675920
- 3 [11] Q. Zhang, et al., Electrochemical model of lithium-ion battery for wide
4 frequency range applications, Electrochim. Acta, Vol. 343, 2020, doi:
5 10.1016/j.electacta.2020.136094
- 6 [12] S. Nejad, D.T. Gladwin, D.A. Stone, A systematic review of lumped-
7 parameter equivalent circuit models for real-time estimation of lithium-
8 ion battery states, J. Power Sources, Vol. 316, 2016, 183–196, doi:
9 10.1016/j.jpowsour.2016.03.042
- 10 [13] Y. Wang, et al., Probability based remaining capacity estimation using
11 data-driven and neural network model, J. Power Sources, Vol. 315, 2016,
12 199–208, doi: 10.1016/j.jpowsour.2016.03.054
- 13 [14] E.L. de Angelis, et al., Terminal height estimation using a Fading Gaus-
14 sian Deterministic filter, Aerosp. Sci. Technol., Vol. 55, 2016, 366–376,
15 doi: 10.1016/j.ast.2016.06.013
- 16 [15] Y. Wang, et al., A comprehensive review of battery modeling and state
17 estimation approaches for advanced battery management systems, Re-
18 newable and Sustainable Energy Reviews, Vol. 131, 2020, 1–18, doi:
19 10.1016/j.rser.2020.110015
- 20 [16] W. Peukert, Über die Abhängigkeit der Kapazität von der Entla-
21 destromstärke bei Bleiakкумуляtoren, Elektrotechnische Zeitschrift,
22 Vol. 20, 1897, 20–21.

- 1 [17] L.W. Traub, Range and Endurance Estimates for Battery-Powered
2 Aircraft, *J. Aircraft*, Vol. 48, No. 2, March 2011, 703–707, doi:
3 10.2514/1.C031027
- 4 [18] G. Avanzini, F. Giulietti, F., Maximum Range for Battery-Powered
5 Aircraft, *J. Aircraft*, Vol. 50, No. 1, Jan. 2013, pp. 304-307; doi:
6 10.2514/1.C031748
- 7 [19] L.W. Traub, Validation of endurance estimates for battery powered
8 UAVs, *Aeronautical Journal*, Vol. 117, No. 1197, 2013, 1155–1166, doi:
9 10.1017/S0001924000008757
- 10 [20] M. Gatti, F. Giulietti, M. Turci, Maximum Endurance for Battery-
11 Powered Rotary-Wing Aircraft, *Aerosp. Sci. Technol.*, Vol. 45, 2015,
12 174–179, doi: 10.1016/j.ast.2015.05.009
- 13 [21] P. Lindahl, I. Moog, S.R. Shaw, Simulation, design, and validation of
14 an UAV SOFC propulsion System, *IEEE Trans. Aerosp. Electron. Syst.*,
15 Vol. 48, No. 3, 2012, 2582–2591, doi: 10.1109/TAES.2012.6237610
- 16 [22] E.S. Latorre, Propulsion system optimization for an unmanned light
17 weight quadrotor (dissertation), Universitat Politècnica de Catalunya,
18 Barcelona, 2011.
- 19 [23] D. Kaya, et al., Propulsion system selection and modeling for a quadro-
20 tor with search and rescue mission, 54th AIAA Aerospace Sciences Meet-
21 ing, Jan. 4-8, 2016, Reston, California, 1–10, 10.2514/6.2016-1528
- 22 [24] A. Abdilla, A. Richards, S. Burrow, Power and endurance modelling of
23 battery-powered rotorcraft, 2015 IEEE/RSJ International Conference

- 1 on Intelligent Robots and Systems (IROS), Sept. 28–Oct. 2, 2015, Ham-
2 burg, Germany, 675–680, doi: 10.1109/IROS.2015.7353445
- 3 [25] A. Abdilla, A. Richards, S. Burrow, Endurance optimization of battery-
4 powered rotorcraft, Towards Autonomous Robotic systems, 16th An-
5 nual Conference, Sept 8–10, 2015, Liverpool, England, 1–12, doi:
6 10.1007/978-3-319-22416-9
- 7 [26] M.E. Fuller, A Battery Model for Constant–Power Discharge Including
8 Rate Effects, Energy Conversion and Management, Vol. 88, 2014, 199–
9 205, doi: 10.1016/j.enconman.2014.08.015
- 10 [27] G. Avanzini, E.L. de Angelis, F. Giulietti, Optimal performance and
11 sizing of a battery–powered aircraft, Aerosp. Sci. Technol., Vol. 59, 2016,
12 132–144, doi: 10.1016/j.ast.2016.10.015
- 13 [28] M. Cerny, C. Breitsamter, Investigation of small–scale propellers under
14 non–axial inflow conditions, Aerosp. Sci. Technol., Vol. 106, Nov. 2020,
15 1–14, doi: 10.1016/j.ast.2020.106048
- 16 [29] G. Gupta, S. Abdallah, Propeller Force–Constant Modeling for Mul-
17 tirotor UAVs from Experimental Estimation of Inflow Velocity, In-
18 ternational J. Aerospace Engineering, Vol. 2018, 2018, 1–10, doi:
19 10.1155/2018/9632942
- 20 [30] S. Delbecq, et al., Efficient sizing and optimization of multirotor drones
21 based on scaling laws and similarity models, Aerosp. Sci. Tecnol.,
22 Vol. 102, July 2020, 1–23, doi: 10.1016/j.ast.2020.105873

- 1 [31] D. Shukla, N. Komerath, Multirotor Drone Aerodynamic Interaction
2 Investigation, *Drones*, Vol. 2, No. 43, 2018, 1–13, doi: 10.3390/
3 drones2040043
- 4 [32] N.A. Vu, D.K. Dang, T. Le Dinh, Electric propulsion system siz-
5 ing methodology for an agriculture multicopter, *Aerosp. Sci. Technol.*,
6 Vol. 90, 2019, 314–326, doi: 10.1016/j.ast.2019.04.044
- 7 [33] H. Zhu, et al., Design and assessment of octocopter drones with im-
8 proved aerodynamic efficiency and performance, *Aerosp. Sci. Technol.*,
9 Vol. 106, Nov. 2020, 1–16, doi: 10.1016/j.ast.2020.106206
- 10 [34] D.M. Filatov, A.V. Devyatkin, A.I. Friedrich, Quadrotor parameters
11 identification and control system design, 2017 IEEE Conference of
12 Russian Young Researchers in Electrical and Electronic Engineering
13 (EIconRus), Feb. 1–3, St. Petersburg, Russia, 2017, 826–830, doi:
14 10.1109/EIconRus.2017.7910684
- 15 [35] C.E. Tinney, J. Sirohi, Multirotor Drone Noise at Static Thrust, *AIAA*
16 *Journal*, Vol. 56, No. 7, July 2018, 2816–2826, doi: 10.2514/1.J056827
- 17 [36] Z.J. Chen, A. Stol, P.J. Richards, Preliminary design of multirotor UAVs
18 with tilted-rotors for improved disturbance rejection capability, *Aerosp.*
19 *Sci. Technol.*, Vol. 92, 2019, 635–643, doi: 10.1016/j.ast.2019.06.038
- 20 [37] E.V. Loureiro, et al., Evaluation of low fidelity and CFD methods for
21 the aerodynamic performance of a small propeller, *Aerosp. Sci. Technol.*,
22 Vol. 108, Jan. 2021, 1–17, doi: 10.1016/j.ast.2020.106402

- 1 [38] B.W. McCormick, *Aerodynamics, Aeronautics, and Flight Mechanics*,
2 2nd Edition, John Wiley & Sons, Inc., New York, 1994, 413–419.
- 3 [39] J.G. Leishman, *Principles of Helicopter Aerodynamics*, 2nd Edition,
4 Cambridge University Press, New York, 2006, Chs. 2 and 5.
- 5 [40] R.W. Deters, G.K. Ananda, M.S. Selig, Reynolds Number Effects
6 on the Performance of Small-Scale Propellers, 32nd AIAA Applied
7 Aerodynamics Conference, June 16–20, Atlanta, GA, 2014, 1–43, doi:
8 10.2514/6.2014-2151
- 9 [41] M. Wang, et al., Battery package design optimization for small electric
10 aircraft, *Chinese Journal of Aeronautics*, Vol. 33, No. 11, 2020, 2864–
11 2876, doi: 10.1016/j.cja.2020.04.021
- 12 [42] Z. Ma, et al., Convex modeling for optimal battery sizing and control
13 of an electric variable transmission powertrain, *Oil & Gas Science and*
14 *Technology*, Vol. 74, No. 25, 2019, 1–13, doi: 10.2516/ogst/2018104
- 15 [43] X.Z. Gao, et al., Joint optimization of battery mass and flight trajec-
16 tory for high-altitude solar-powered aircraft, *Proc. of the Institution of*
17 *Mechanical Engineers, Part G*, Vol. 228, No. 13, 2014, 2439–2451, doi:
18 10.1177/0954410013518510
- 19 [44] W. Johnson, *Helicopter Theory*, Dover Publications, Inc., New York,
20 1994, 299–300.
- 21 [45] A. Gong, R. MacNeill, D. Verstraete, Performance Testing and Modeling
22 of a Brushless DC Motor, Electronic Speed Controller and Propeller for

- 1 a Small UAV, AIAA 2018–4584, 2018 Joint Propulsion Conference, July
- 2 9–11, Cincinnati, Ohio, 2018, 1–15, doi: 10.2514/6.2018-4584
- 3 [46] A.M. Harrington, C. Kroninger, Characterization of Small DC Brushed
- 4 and Brushless Motors, USA Army Research Laboratory Tech. Report
- 5 ARL–TR–6389, 2013, 1–48
- 6 [47] Solutions for All Markus Müller, eCalc - The most reliable RC Calculator
- 7 on the Web, Retrieved from <https://www.ecalc.ch>, 2021.
- 8 [48] C. Persson, Drive Calculator, Retrieved from <http://www.drivecalc.de>,
- 9 2021.
- 10 [49] C.N. Keys, Rotary-Wing Aerodynamics - Volume II - Performance Pre-
- 11 diction of Helicopters, NASA Contractor Report 3083, Jan. 1979, Ch. 2.
- 12 [50] I.H. Abbott, A.E. Von Doenhoff, Theory of wing sections, Dover Publi-
- 13 cations, Inc., New York, 1959, Ch. 5.
- 14 [51] S.F. Hoerner, Fluid Dynamic Drag: Practical Information on Aerody-
- 15 namic Drag and Hydrodynamic Resistance, Hoerner Fluid Dynamics,
- 16 Published by the Author, Bakersfield, CA, 1965, Ch. 2.
- 17 [52] D. Sartori, W. Yu, Experimental Characterization of a Propulsion Sys-
- 18 tem for Multi-rotor UAVs, J. Intell. Robot. Syst., Vol. 96, 2019, 529–540,
- 19 doi: 10.1007/s10846-019-00995-2
- 20 [53] DJI, Professional, Enterprise, and Agriculture Drones, Retrieved from
- 21 <https://www.dji.com>, 2021.

- 1 [54] FreeFly Systems, Professional Drones, Retrieved from [https://www.](https://www.freeflysystems.com)
2 [freeflysystems.com](https://www.freeflysystems.com), 2021.
- 3 [55] Yuneec, Yuneec Drones for Commercial Use, Retrieved from [https://](https://www.yuneec.com)
4 www.yuneec.com, 2021.
- 5 [56] RC Timer, Commercial/Industrial Propellers, Retrieved from [https://](https://www.rctimer.com/commercial-industrial-propellers-c0420)
6 www.rctimer.com/commercial-industrial-propellers-c0420, 2021.
- 7 [57] T-Motor, Carbon Fiber and Polymer Propellers, Retrieved from [ht](https://store-en.tmotor.com/category.php?id=4)
8 [tps://store-en.tmotor.com/category.php?id=4](https://store-en.tmotor.com/category.php?id=4), 2021.
- 9 [58] W.H. Press, et al., Numerical recipes: the art of scientific computing -
10 2nd Edition, Cambridge University Press (1992), Chs. 5, 9, and 10.
- 11 [59] R.P. Brent, Algorithms for minimization without derivatives, Prentice-
12 Hall (2013), Ch. 5.
- 13 [60] D. Curtiss, Recent extensions of Descartes' rule of signs, Annals of Maths
14 Vol. 19, No. 4, 1918, 251–278.
- 15 [61] M. Gatti, Complete Preliminary Design Methodology for Electric Mul-
16 tirotor, J. Aerosp. Eng., Vol. 30, Issue 5, 2017, 1–15, doi: 10.1061/
17 (ASCE)AS.1943-5525.0000752
- 18 [62] DJI, E2000–Tuned Propulsion System, Retrieved from [https://www.](https://www.dji.com/en/e2000)
19 [dji.com/en/e2000](https://www.dji.com/en/e2000), 2021.
- 20 [63] M. Biczyski, et al., Multicopter Sizing Methodology with Flight Time
21 Estimation, J. Advanced Transportation, Vol. 2020, 2020, 1–15, doi:
22 10.1155/2020/9689604

- ¹ [64] T-Motor, U8 KV135 Efficiency Type, Retrieved from [https://store-](https://store-en.tmotor.com/goods.php?id=323)
² [en.tmotor.com/goods.php?id=323](https://store-en.tmotor.com/goods.php?id=323), 2021.
- ³ [65] Tattu Batteries, Retrieved from <https://www.genstattu.com>, 2021.